Supporting information

The Grain Morphology and Surface Properties of Li-Rich Li_2MnO_3 Cathode Material

Xiaotong Yan, Xingyu Zhou, Chunwei Zhu, Weijie Huang, Yu-Jun Zhao *

Department of Physics, South China University of Technology, Guangzhou 510641, PR China

S1. Crystal structures

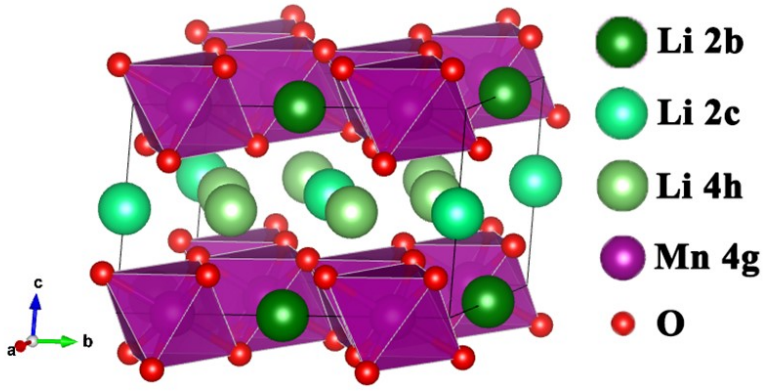

Fig. S1. Crystal structure of Li_2MnO_3, by VESTA.[1]

* Corresponding author.
E-mail address: zhaoyj@scut.edu.cn (Y.-J. Zhao).

S2. Thermodynamic analysis of the system

In this study, the compound, space groups, total energy E_{ele} of the DFT calculation, and zero-point vibrational energy (ZPE) are listed in Table S1. Note that due to the overestimation of the binding energy of oxygen in the DFT calculation, the free energy of oxygen is corrected in the calculation process (total energy E_{ele} of oxygen is equal to the energy of two isolated oxygen atoms plus the experimentally measured binding energy -5.23 eV [2]), and its accuracy is demonstrated by comparing the reaction enthalpy of the reaction between lithium and oxygen to produce Li_2O, as shown in Table S2.

Table S1. The compound, space groups, E_{ele} and ZPE (in per formula unit).

Compound	Space group	E_{ele} (eV)	ZPE (eV)
Li_2MnO_3	C2/m	-36.563	0.430
Li_2O	$Fm\bar{3}m$	-14.314	0.233
MnO_2	Pnma	-20.779	0.221
Li	$Fm\bar{3}m$	-1.897	0.042
Mn	$I\bar{4}3m$	-6.544	0.025
O	Gas Phase	-9.05	0.11

Table S2. The comparison of calculational and experimental enthalpy of Li_2O.

	Calculation (eV)	Experiment (eV) [3]
ΔH	-5.901	-6.140

The chemical potential $\mu_O(T,P)$ of oxygen under air conditions is shown in Table S3.

Table S3. The chemical potential $\mu_O(T,P)$ of oxygen under air conditions.

T (K)	$\mu_O(T,P)$ (eV)	T (K)	$\mu_O(T,P)$ (eV)
0	-4.470	1100	-5.771
100	-4.552	1200	-5.907
200	-4.653	1300	-6.043
300	-4.764	1400	-6.182
400	-4.880	1500	-6.322
500	-5.000	1600	-6.464
600	-5.121	1700	-6.605
700	-5.247	1800	-6.749
800	-5.375	1900	-6.894
900	-5.506	2000	-7.039
1000	-5.637	2100	-7.186

Generally, the atomic vibrational free energy values at the different sites of the same element are different because of the different Wyckoff positions (different coordination environments) occupied. Therefore, As shown in Fig. S1, for the Li_2MnO_3, the phonon density of states and the atomic free vibrational energy of the different elements are shown in Fig. S2.

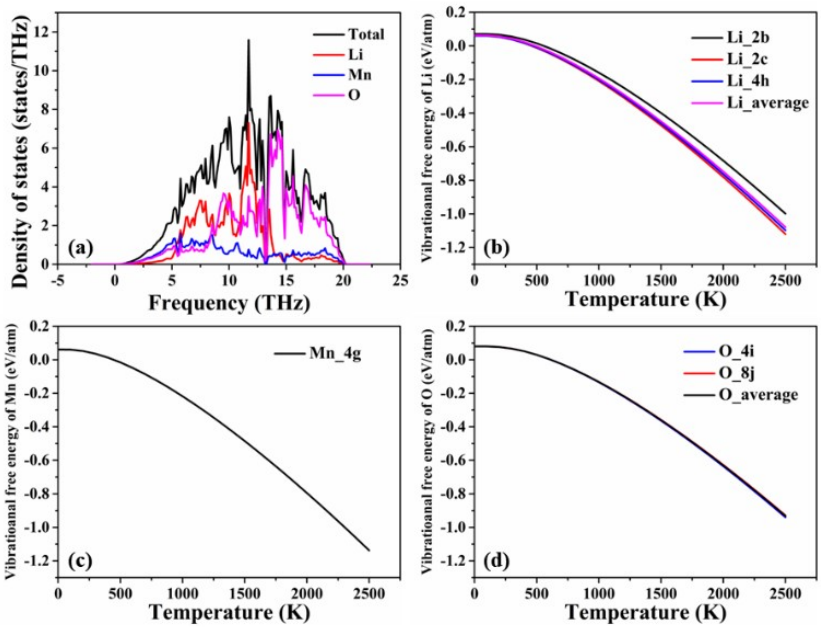

Fig. S2. (a) The total phonon density of states of Li_2MnO_3 and the partial phonon density of states of differential elements. (b) The vibrational free energy of Li atoms at different sites and their average values. (c) The Vibrational free energy of the atom of Mn. (d) The vibrational free energy of the O atoms at different positions and their average values.

From Fig. S2(a) it can be seen that the vibrational mode of the oxygen atoms has a higher vibrational frequency, followed by the Li atoms, while the vibrational frequency of the Mn atoms is almost evenly distributed over the entire vibrational mode. In addition, as can be seen from Fig. S2 (b), (c) and (d), for the convenience of calculation, the vibration free energy of the same atom at different Wyckoff positions can be approximately replaced by its average value.

S3. Linear regression analysis

The surface energy E_{Surf} of Li_2MnO_3 is supposed as linear function of the density of cleaved bond and bond type:

$$E_{Surf} = n_{Li-O}x + n_{Mn-o}y + z \quad (1)$$

The n_{m-o} (m = Li and Mn) is the density of bonds of different surfaces and terminal, x and y represent the bond strength of Li-O and Mn-O bonds, respectively. The z is the intercept of the linear model. For Li_2MnO_3, there are S ($S \geq 2$) data sets that form the data group N that is trained to predict the surface energy. The density of the bonds n_{m-o} can be written in matrix form:

$$N = \begin{pmatrix} n_{Li-O}^{1} & n_{Mn-O}^{1} & 1 \\ n_{Li-O}^{2} & n_{Mn-O}^{2} & 1 \\ \vdots & \vdots & \vdots \\ n_{Li-O}^{S} & n_{Mn-O}^{S} & 1 \end{pmatrix} \quad (2)$$

Meanwhile, the bond strength (x and y) and intercept (z) are also composed a vector $X = (x,y,z)^T$, the function (1) can be expressed in matrix form:

$$Y = NX \quad (3)$$

The $Y = (E_{Surf}^{1}, E_{Surf}^{2}, \ldots, E_{Surf}^{S})^T$ represents the surface energy of N surfaces for Li_2MnO_3 by DFT calculation. The X in the above equation is solved by using the least-squares method. For the accuracy judgment of the above methods, the correlation coefficient r is used:

$$r = \frac{\sum (\hat{E}_{Surf}^{S} - \bar{\hat{E}}_{Surf})(E_{Surf}^{S} - \bar{E}_{Surf})}{\sum (\hat{E}_{Surf}^{S} - \bar{\hat{E}}_{Surf})^2 \sum (E_{Surf}^{S} - \bar{E}_{Surf})^2} \quad (4)$$

Here, E_{Surf}^{S} and $\bar{E}_{Surf}$ represent the surface energy of the S-th surface after the calculation of DFT and its average value, respectively. $\hat{E}_{Surf}^{S}$ and $\bar{\hat{E}}_{Surf}$ represent the surface energy of the S-th surface by linear fitting and its average value, respectively.

In this study, with the available computing resources, there are three groups' data be used for training:

(1) Surface energy of (101), $(10\bar{1})$, (011), (010), and (111) surfaces that satisfy

the stoichiometric ratios, recorded as Miller_1.

(2) Surface energy of (101), $(10\bar{1})$, (011), (010), (111), and (131) that satisfy the stoichiometric ratios, recorded as Miller_1_131.

(3) Surface energy of the surfaces of (101), $(10\bar{1})$, (011), (010), (111), (131) and (120) that satisfy the stoichiometric ratios, recorded as Miller_1_131_120.

The comparison between the surface energy obtained by linear fitting of the above three groups of data and the real surface energy obtained by DFT calculation is shown in Fig. S3, and the corresponding values of X and r are shown in Table S4.

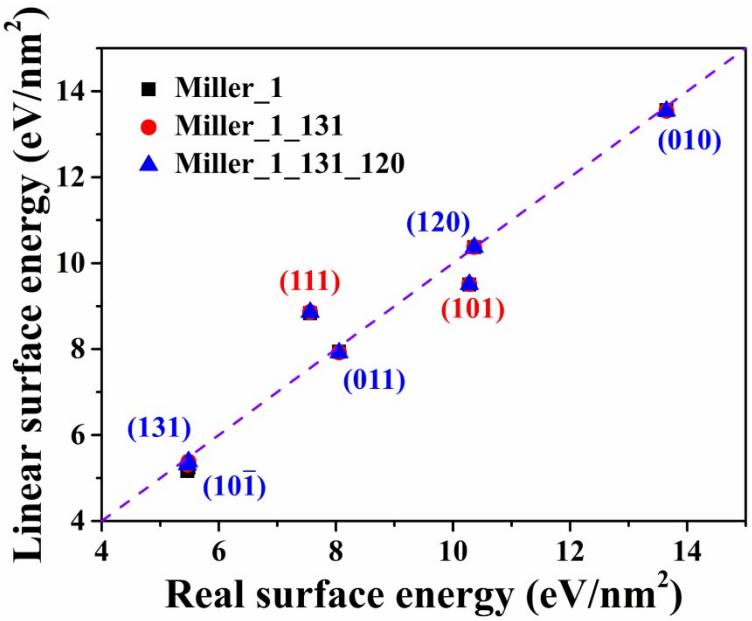

Fig. S3. The comparison of surface energy values between linear fitting prediction and DFT calculation.

Table S4. The values of vector $X = (x,y,z)^T$ and correlation coefficient r.

	Miller_1 (eV)	Miller_1_131 (eV)	Miller_1_131_120 (eV/nm^2)
x	0.217	0.204	0.204
y	0.930	0.913	0.913
z	-5.755	-5.263	-5.255
r	0.970	0.976	0.977

According to Fig. S3, except for the difference between the surface energy data

obtained by linear fitting of (111) and (101) and the values calculated by DFT, a reliable surface energy fit can be obtained by applying the linear fitting method for other crystal surfaces. As shown in Table S4, with the addition of surfaces (131) and (120), *x*, *y*, and *z* approach 0.204, 0.913, and -5.255, respectively, and the correlation coefficient *r* also improves slightly. In summary, in order to predict surface energy more accurately, the third set of data Miller_1_131_120 is used.

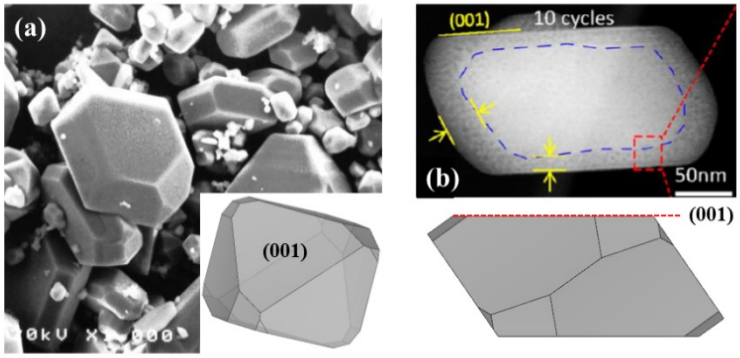

Fig. S4. The Scanning Electron Microscope images of single-crystalline Li_2MnO_3.[4,5]

S4 Surface structure and Naming

Surface Naming Convention:

Format: (crystal face index)_the elements and average atomic quantities (Li, Mn and O).

The average atomic quantities are the average distribution of the remaining atomic numbers at the two terminals of the surface structure after subtracting the corresponding atomic numbers that satisfy the maximum stoichiometric ratio from the atomic numbers of each element in the surface structure. In addition, STO stands for the fulfillment of the stoichiometric ratio.

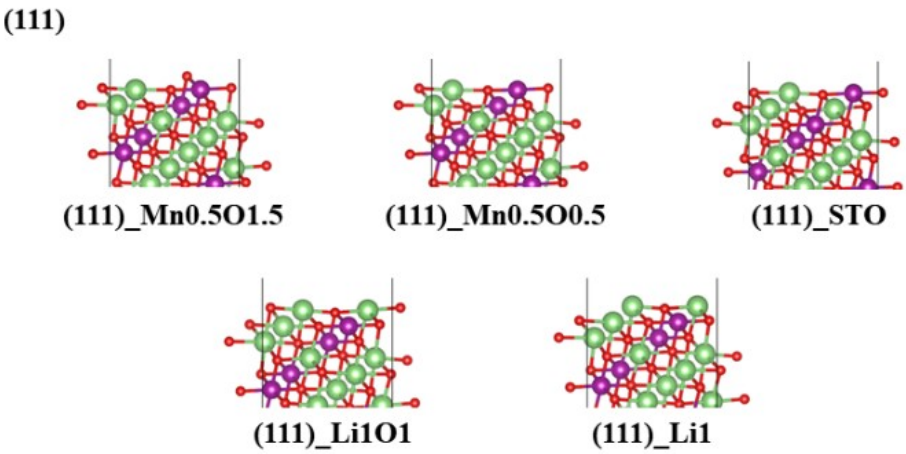

Fig. S5. Surface structures of all the terminations of (111) surface (Green: Li; Purple: Mn; Red: O).

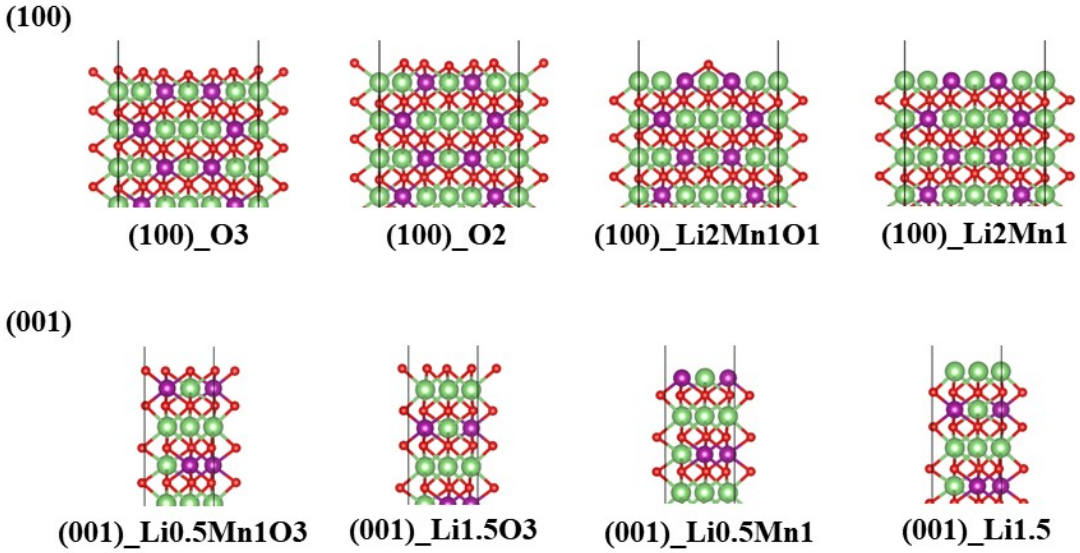

Fig. S6. Surface structures of all the terminations of (100) and (001) surface (Green: Li; Purple: Mn; Red: O).

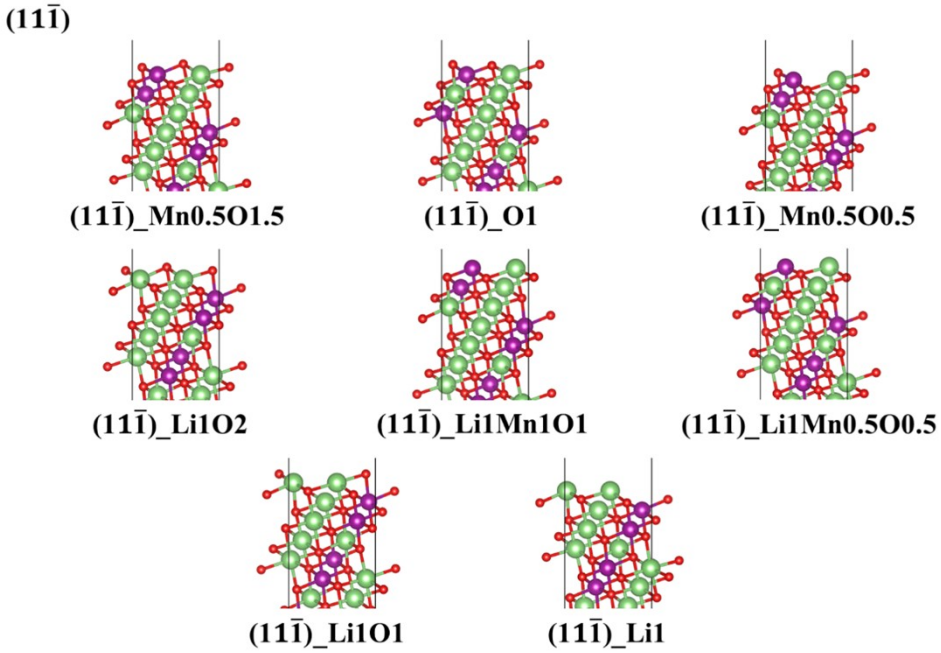

Fig. S7. Surface structures of all the terminations of $(11\bar{1})$ surface (Green: Li; Purple: Mn; Red: O).

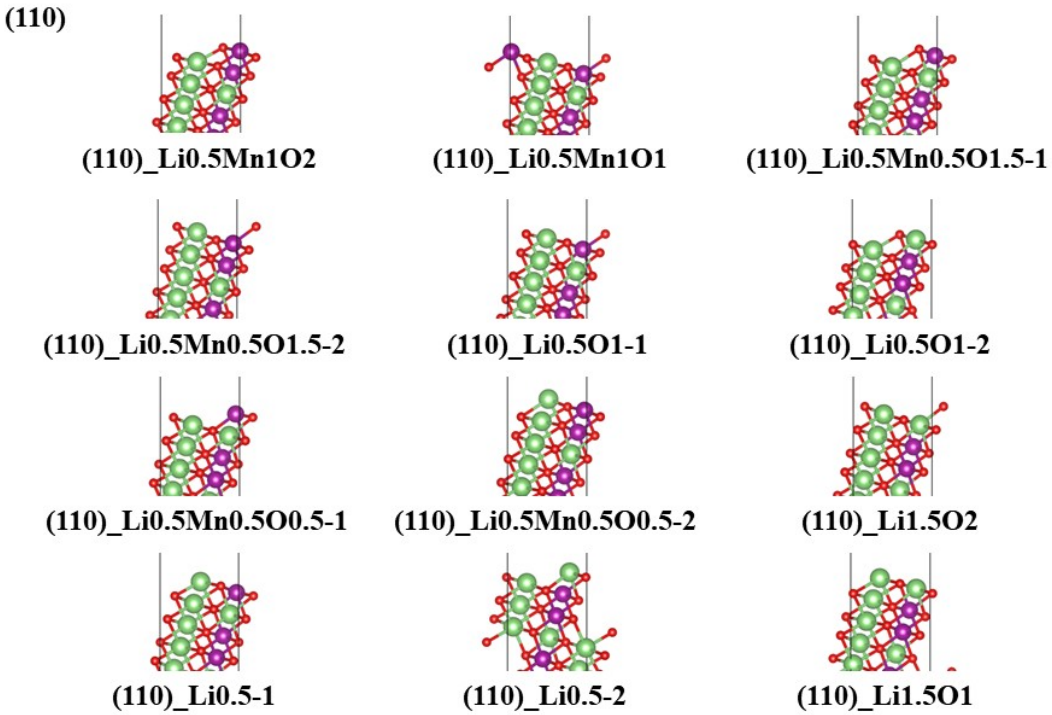

Fig. S8. Surface structures of all the terminations of (110) surface (Green: Li; Purple: Mn; Red: O).

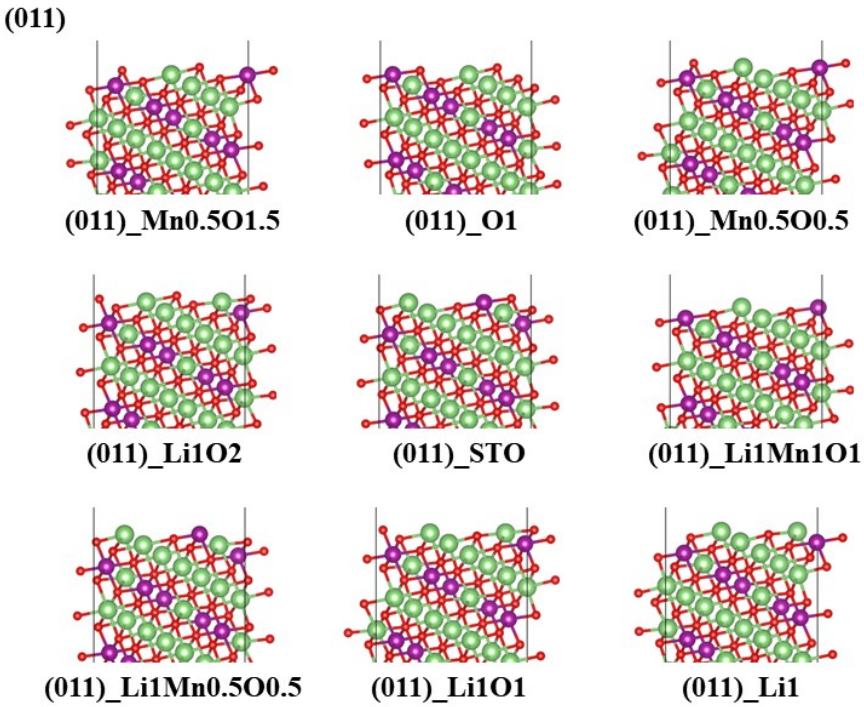

Fig. S9. Surface structures of all the terminations of (011) surface (Green: Li; Purple: Mn; Red: O).

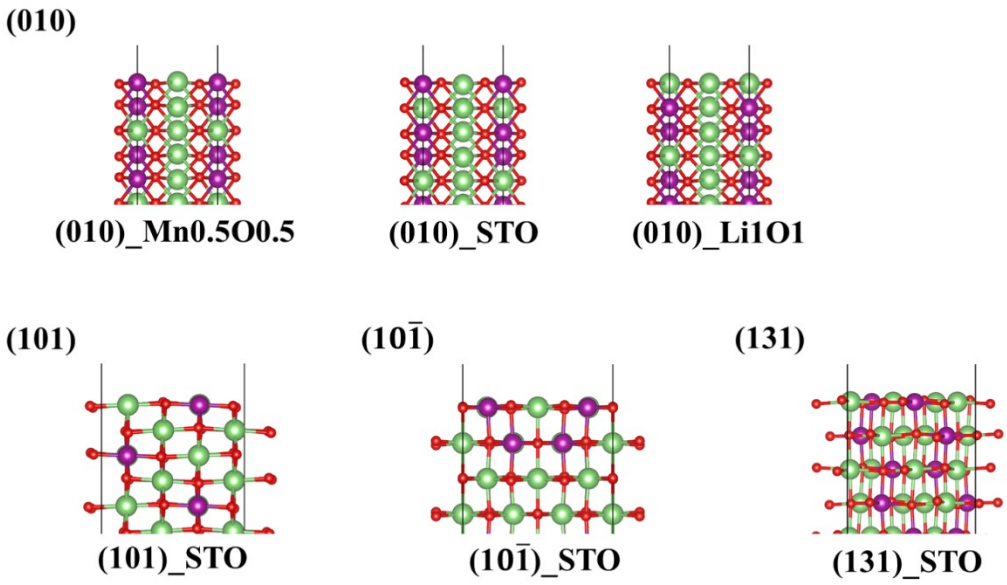

Fig. S10. Surface structures of all the terminations of (010) surface, and surface structures that satisfy stoichiometric ratios of (101), $(10\bar{1})$ and (131) surfaces (Green: Li; Purple: Mn; Red: O).

S5 Stable surface of different terminals on (100), (110), and $(11\bar{1})$ surfaces

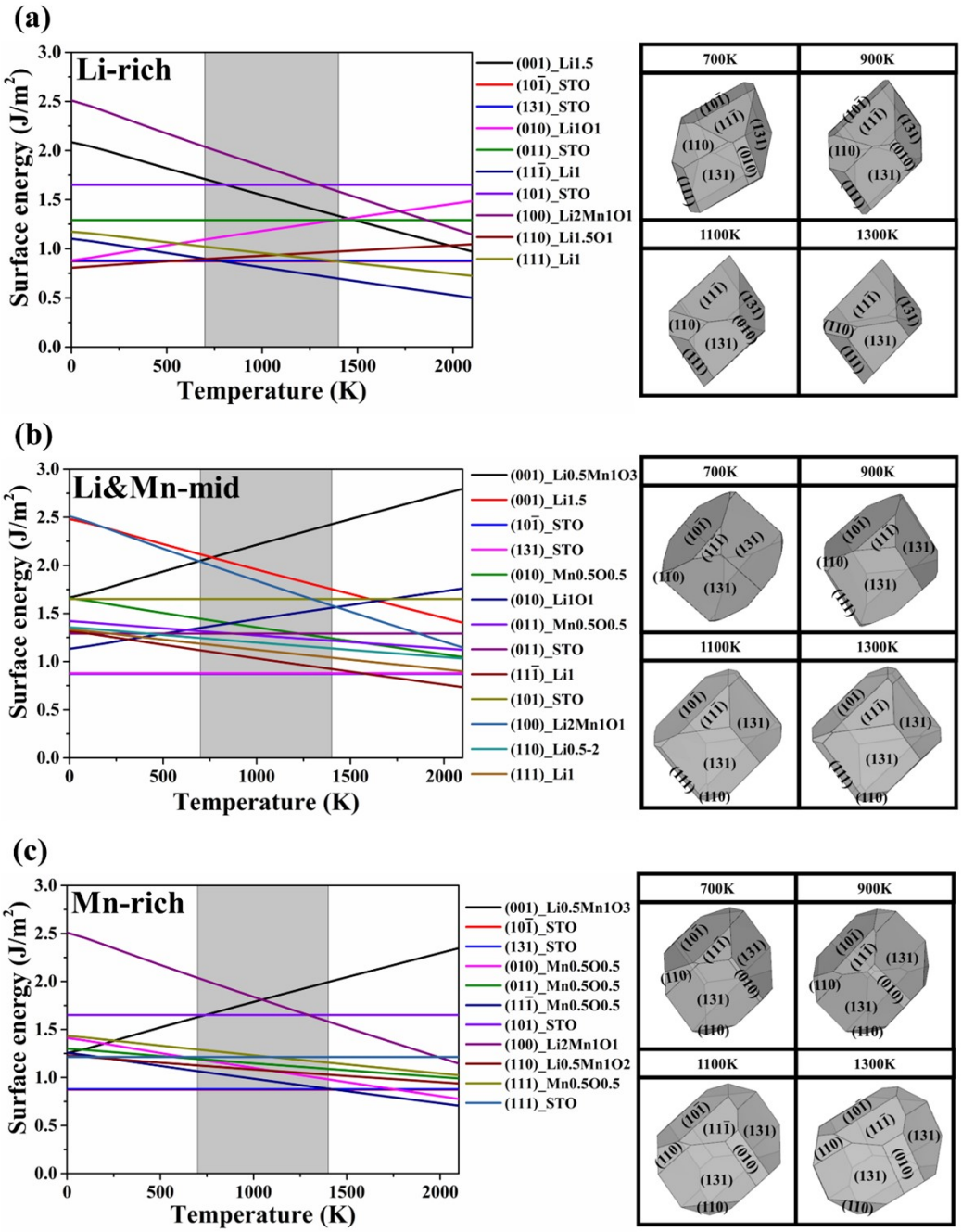

Fig. S11. The change of stable surfaces energy of Li_2MnO_3 at different temperatures and different chemical potentials of Li and Mn, as well as the corresponding Wulff shape (the gray shading marks the main experimental temperature window for synthesis of Li_2MnO_3).[6]

This is evident from Fig. S6-S8 and Fig. S11. For the (100) surface, at the main synthesis temperature is only the (100)_Li2Mn1O1 terminal surface. Thus, combining

with the configuration of each atom in the bulk structure model, where the number of O atoms on the (100)_Li2Mn1O1 surface are added to construct the terminal surfaces that satisfy the stoichiometric ratio. Similarly, for the (110) surface, (110)_Li1.5O1, (110)_Li0.5-2 and (110)_Li0.5Mn1O2 are the stable surfaces at all synthesis temperatures and chemical potentials. Thus, in combination with the (110)_Li0.5-2 surface and bulk structure, the number of Li ions on the (110)_Li0.5-2 surface (is a (2 × 1 × 1) supercell structure) are removed to provide the surfaces that meet the stoichiometric requirement. Finally, for the $(11\bar{1})$ surface, the $(11\bar{1})$_Li1 and $(11\bar{1})$_Mn0.5O0.5 surfaces are stable at all experimental temperatures, from the Li-rich environment to the Mn-rich environment. Therefore, the number of Li atoms on the $(11\bar{1})$_Li1 terminal surface are removed to meet the stoichiometric ratio. The stable surface structures of (100), (110), and $(11\bar{1})$ that satisfy the stoichiometric ratio are shown in Fig. S12.

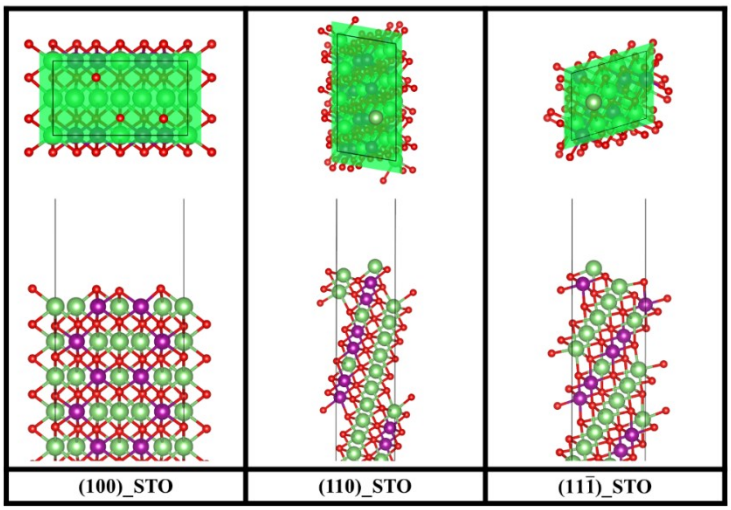

Fig. S12. The stable surface structures that satisfy stoichiometric ratios of (100), (110), and $(1\bar{1}\bar{1})$ surfaces.

The change of surface energy of different terminal surfaces (including stoichiometric surfaces) of (100), (110) and $(1\bar{1}\bar{1})$ surfaces, under different temperatures and chemical potential conditions are shown in Fig. S13. For the (100) surface, when the temperature is below 1355 K, the (100)_STO surface has the lowest surface energy. This indicates that the (100)_STO surface is most stable surface compare with other (100) surfaces under almost the entire experimental synthesis temperatures. However, based on the analysis of Fig. S13 and Fig. 4 in the main text, it can be seen that the (100) surface do not appear as stable surfaces in the Wulff shape due to their higher surface energy compared to other low Miller index surfaces (the (100)_Li2Mn1O1 terminal with slightly lower surface energy is also considered). For surfaces (110) and $(1\bar{1}\bar{1})$, the surfaces that satisfy the stoichiometric ratio ((110)_STO and $(1\bar{1}\bar{1})$_STO) do not have the lowest surface energy at the synthesis temperatures, which do not appear in all synthesis environments.

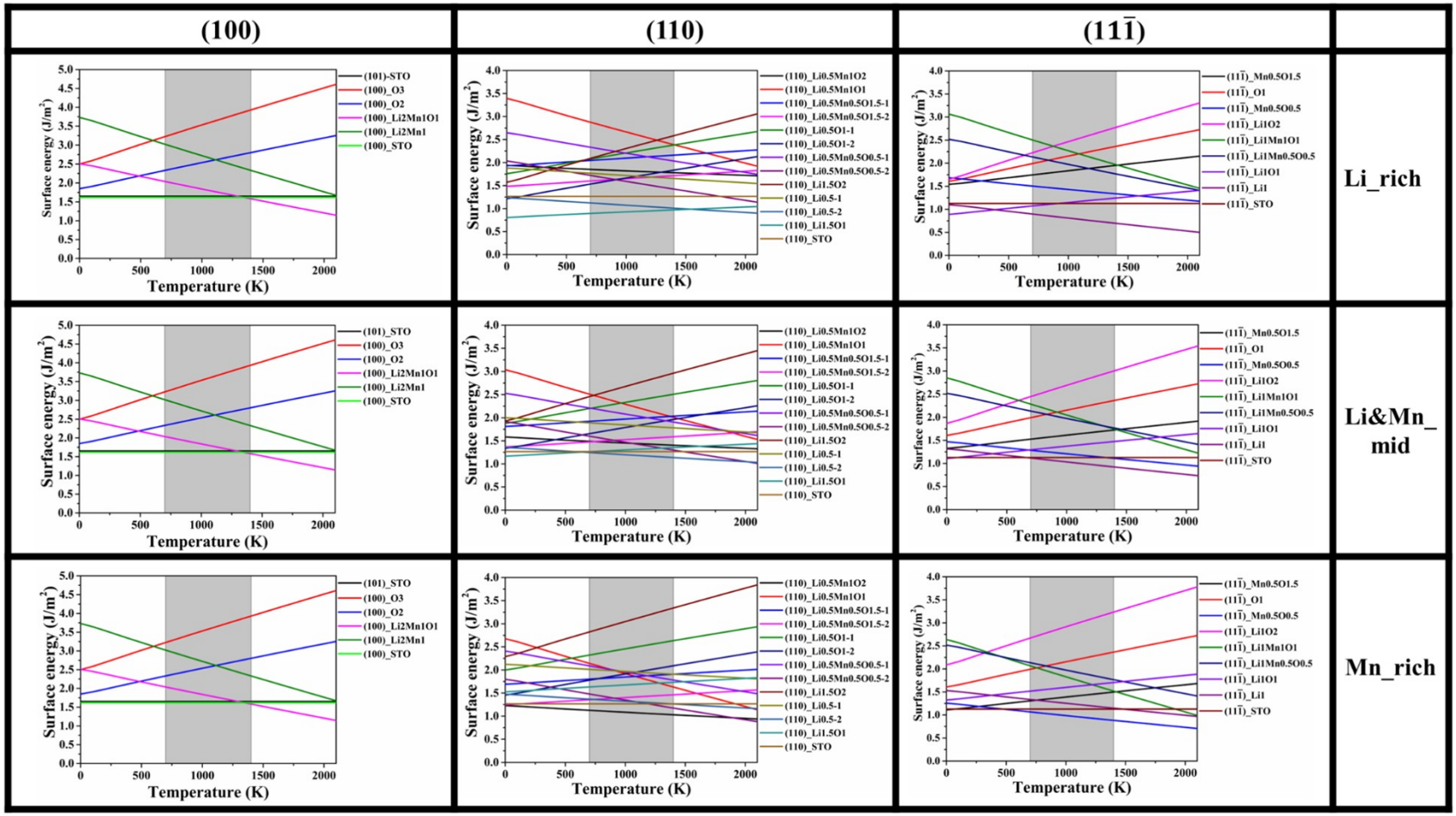

Fig. S13. The change of surfaces energy of (100), (110), and $(11\bar{1})$ surfaces of Li_2MnO_3 at different temperatures and different chemical potentials of Li and Mn (the gray shading marks the main experimental temperature window for synthesis and sintering of Li_2MnO_3).

S6 Determination of the Surface Influence Zone (SIZ) of Li_2MnO_3

Fig. S14 shows the average, maximum, and minimum values of integrated crystal orbital Hamilton population (ICOHP) [7,8] for Li-O and Mn-O as a function of depth from different surfaces and terminals, and compares them with the corresponding range of changes in ICOHP of the bulk structure.

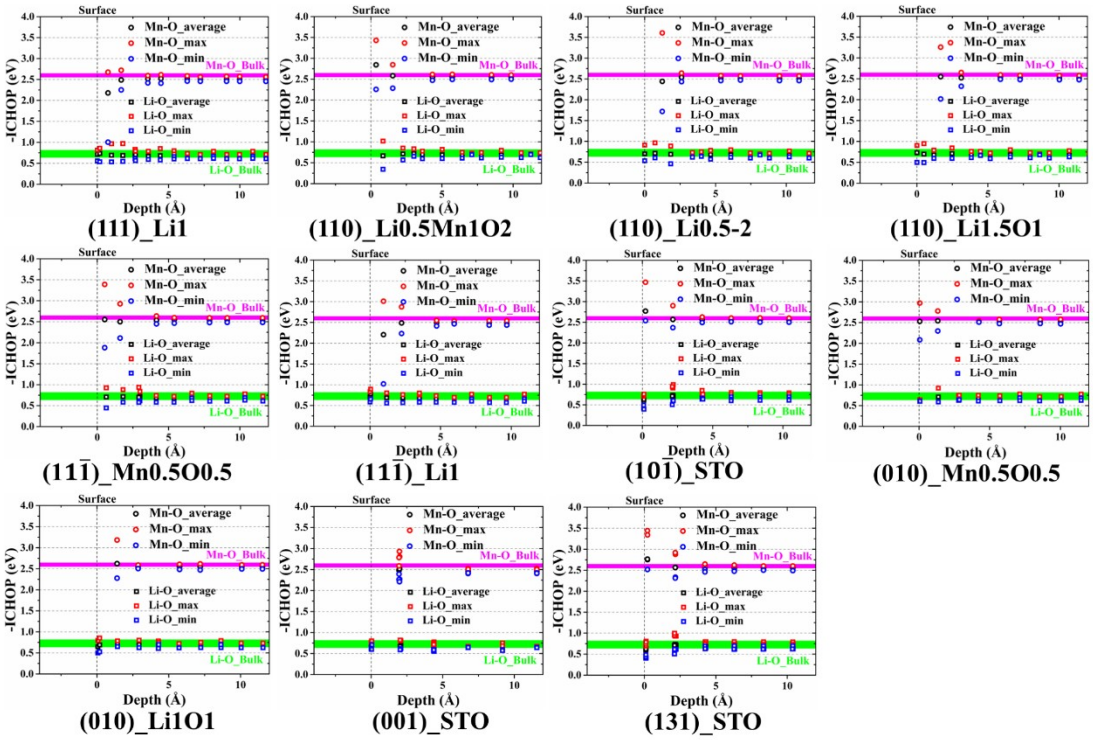

Fig. S14. The -ICHOP at different depths from different surfaces and terminals of Li_2MnO_3, and comparison with bulk structure.

From Fig. S14, it can be seen that the ICOHP values of Mn-O and Li-O on different surfaces and terminals gradually approach the corresponding values of the bulk structure with increasing depth, indicating that the performance of the system transitions from a surface-dominated to a bulk-dominated structure with increasing surface depth. For the bulk structure of Li_2MnO_3, the -ICOHP of Mn-O has higher values than the -ICOHP of Li-O, with the average value exceeding three times. This

indicates that the Mn-O bond has a higher bond strength compared to the Li-O bond. Moreover, the electrostatic potential of the oxygen site at different depths from different surfaces and terminals of Li_2MnO_3, as shown in Fig. S15.

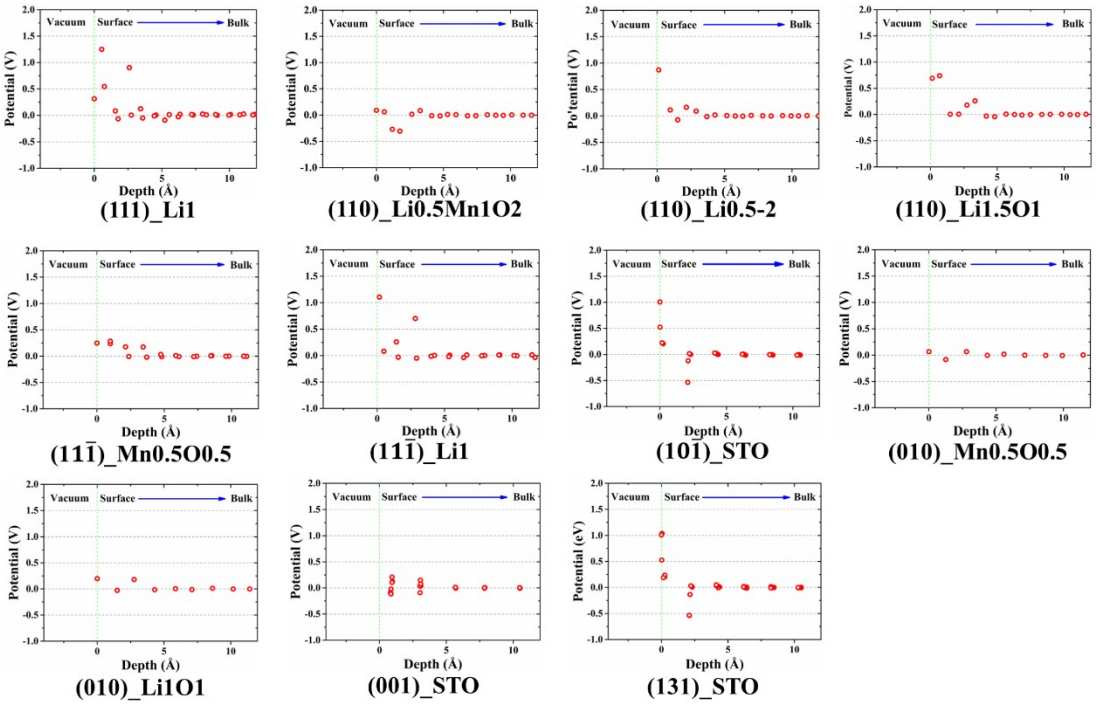

Fig. S15. The oxygen site electrostatic potential at different depths from different surfaces and terminals of Li_2MnO_3.

It can be seen from Fig. S15, similarly, the variation of electrostatic potentials at the oxygen sites with surface depth is similar to that of ICOHP, which shows that with depth increases the electrostatic potential at the oxygen site also tends towards the bulk structure. This also proves that with depth increases, system characteristics evolve from surface dominated to bulk structure dominated. In this work, we mainly study the surface properties of stable terminals, so the main scope of our research is limited to the zone of surface influence. Thus, the trend domain (thickness defined as *d*) that gradually evolves from surface dominance to bulk structure dominance is defined as the surface influence zone. Based on the results of the ICOHP and oxygen site

electrostatic potential, it can be seen that except for the thickness of the surface influence zone of $(10\bar{1})$ _STO, (001)_STO and (131)_STO are 3 Å, all others terminals are 5 Å.

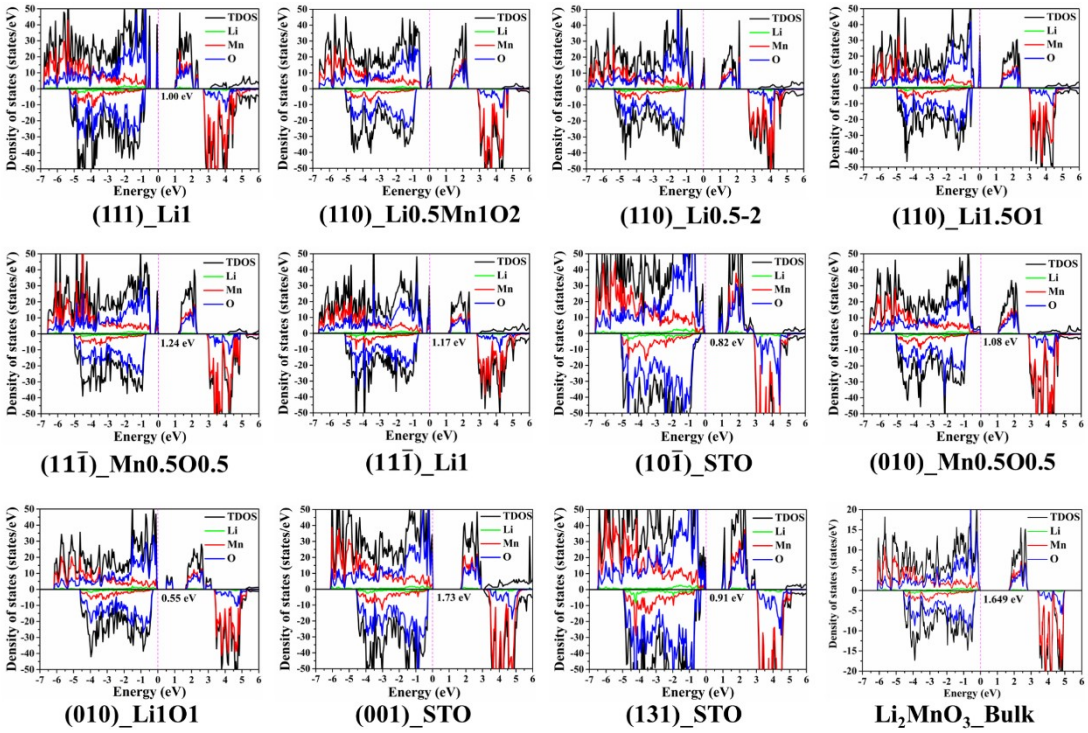

Fig. S16. TDOS and PDOS for different surfaces and terminals of Li_2MnO_3 as well as bulk structure.

S7 Average deintercalation voltages

First-principles calculations are widely used to determine the theoretical electrochemical voltage profile in many compounds.[9,10] According to the established formalism, the average voltage for the extraction of Li ions from a material Li_xHost is given as follows:

$$\bar{V} = \frac{\left|E_{coh}\left[Li_{x_1}Host\right] - E_{coh}\left[Li_{x_2}Host\right] - (x_1 - x_2)E_{coh}[Li]\right|}{(x_1 - x_2)} \quad (5)$$

$E_{coh}[Li_xHost]$ refers to the total energy of the corresponding structures, x_1 and x_2 represent the corresponding amount of Li ions in the corresponding structures, $E_{coh}[Li]$ represents the total energy of the lithium phase primitive cell of the BCC structure.

S8 Oxygen evolutions on the different terminals

The oxygen evolution on each terminal facet is calculated as the oxygen release energy $G_f(T,P)$, In general, the negative oxygen release energy indicates that the oxygen can be easily released, while the positive oxygen release energy means that the oxygen cannot be evolved. The calculation formula is as follows:

$$G_f(T,P) = G_x^{slab}(T,P) + \frac{1}{2}x\mu_O(T,P) - G^{slab}(T,P) \quad (6)$$

The $G^{slab}(T,P)$ and $G_x^{slab}(T,P)$ represent the total energy of the slab structure before and after oxygen release, respectively. x is the number of evolutions of O atoms. The $\mu_O(T,P)$ is the chemical potential of the O molecule. In this study, the temperature (T) and pressure (P) are assumed to be 300 K and 10^{-5} atm, respectively, so the $\mu_O(300\ K, 10^{-5}\ atm)$ is -4.893 eV.

S9 Coordination of various atoms in Li_2MnO_3 bulk structure

Fig. S17. The coordination environment of various atoms in Li_2MnO_3 bulk structure. The green, purple, and red fonts represent the average Hirshfeld-I charges of Li, Mn, and O in the bulk structure, respectively, and the blue font represents the average Hirshfeld-I charges provided by Li ion or Mn ion to surrounding O ions (Green: Li; Purple: Mn; Red: O).

S10 Explanation of grain morphology of Li_2MnO_3

To explain the dish-shape characteristic of preferential growth along the (001) surface of Li_2MnO_3 grain morphology. In this work, the surface energies of different terminals of common surfaces (according to Wulff theory) are calculated under Li-rich, Li&Mn-mid, and Mn-rich chemical potential conditions. The maximum and minimum values and their differences in surface energies of different terminals on common surfaces as a function of main synthesis temperature are shown in Table S5-S7.

Table S5. The variation of minimum, maximum, and their difference in surface energy (J m^{-2}) at different terminals of common surfaces under Li-rich condition.

Surface	700 K			900 K			1100 K			1300 K		
	MIN	MAX	DIFF	MIN	MAX	DIFF	MIN	MAX	DIFF	MIN	MAX	DIFF
(001)	0.955	4.822	3.867	0.955	4.904	3.949	0.955	5.203	4.248	0.955	5.498	4.543
(010)	1.094	2.191	1.096	1.153	2.191	1.038	1.210	2.191	0.981	1.266	2.191	0.925
(11$\bar{1}$)	0.899	2.502	1.604	0.840	2.388	1.548	0.782	2.545	1.763	0.725	2.700	1.975
(110)	0.895	2.876	1.981	0.918	2.733	1.815	0.940	2.594	1.654	0.962	2.515	1.553
(111)	1.022	1.618	0.596	0.978	1.656	0.678	0.935	1.700	0.765	0.892	1.743	0.851
(10$\bar{1}$)	0.873	0.873	—	0.873	0.873	—	0.873	0.873	—	0.873	0.873	—
(131)	0.878	0.878	—	0.878	0.878	—	0.878	0.878	—	0.878	0.878	—

Table S6. The variation of maximum, minimum, and their difference in surface energy (J m^{-2}) at different terminals of common surfaces under Li&Mn-mid condition.

Surface	700 K			900 K			1100 K			1300 K		
	MIN	MAX	DIFF	MIN	MAX	DIFF	MIN	MAX	DIFF	MIN	MAX	DIFF
(001)	0.955	5.020	4.065	0.955	5.330	4.375	0.955	5.633	4.678	0.955	5.932	4.977
(11$\bar{1}$)	1.117	2.449	1.332	1.060	2.611	1.551	1.005	2.771	1.766	0.950	2.928	1.978
(110)	1.245	2.510	1.265	1.214	2.605	1.391	1.183	2.749	1.567	1.152	2.892	1.740
(111)	1.186	1.455	0.269	1.143	1.490	0.347	1.102	1.532	0.431	1.060	1.574	0.514
(10$\bar{1}$)	0.873	0.873	—	0.873	0.873	—	0.873	0.873	—	0.873	0.873	—
(131)	0.878	0.878	—	0.878	0.878	—	0.878	0.878	—	0.878	0.878	—

Table S7. The variation of maximum, minimum, and their difference in surface energy (J m^{-2}) at different terminals of common surfaces under Mn-rich condition.

Surface	700 K			900 K			1100 K			1300 K		
	MIN	MAX	DIFF	MIN	MAX	DIFF	MIN	MAX	DIFF	MIN	MAX	DIFF
(001)	0.955	5.442	4.487	0.955	5.756	4.801	0.955	6.063	5.108	0.955	6.366	5.411
(010)	1.192	2.191	0.999	1.130	2.191	1.061	1.070	2.191	1.121	1.010	2.191	1.181
$(11\bar{1})$	1.066	2.670	1.604	1.013	2.835	1.822	0.960	2.997	2.037	0.909	3.156	2.247
(110)	1.126	2.824	1.698	1.097	2.975	1.878	1.070	3.123	2.053	1.043	3.269	2.226
$(10\bar{1})$	0.873	0.873	—	0.873	0.873	—	0.873	0.873	—	0.873	0.873	—
(131)	0.878	0.878	—	0.878	0.878	—	0.878	0.878	—	0.878	0.878	—

References

1 K. Momma and F. Izumi, *J. Appl. Crystallogr.*, 2011, **44**, 1272.

2 L. Wang, T. Maxisch, and G. Ceder, *Phys. Rev. B*., 2006, **73**, 195107.

3 M.W. Chase, *J. Phys. Chem. Ref. Data.*, 1998.

4 X. Yang, W. Tang, H. Kanoh, and K. Ooi, *J. Mater. Chem.*, 1999, **9**, 2683–2690.

5 P. Yan, L. Xiao, J. Zheng, Y. Zhou, Y. He, X. Zu, S.X. Mao, J. Xiao, F. Gao, J.-G. Zhang, and C.-M. Wang, *Chem. Mater.*, 2015, **27**, 975–982.

6 A. Boulineau, L. Croguennec, C. Delmas, and F. Weill, *Solid State Ion*., 2010, **180**, 1652–1659.

7 V. L. Deringer, A. L. Tchougreeff, and R. Dronskowski, *J. Phys. Chem. A*, 2011, **115**, 5461–5466.

8 R. Nelson, C. Ertural, J. George, V. L. Deringer, G. Hautier, and R. Dronskowski, *J Comput Chem*, 2020, **41**, 1–10.

9 Q. He, B. Yu, Z. Li, and Y. Zhao, *Energy Environ. Mater.*, 2019, **2**, 264–279.

10 K.T. Butler, G. Sai Gautam, and P. Canepa, *Npj Comput. Mater.*, 2019, **5**, 19.